Numerical Simulation of the Navier-Stokes Equations for an F-16A Configuration

G. W. Huband,* D. P. Rizzetta,† and J. J. S. Shang‡
Wright Research and Development Center, Wright-Patterson Air Force Base, Ohio

The results of a numerical simulation are presented for the steady flow over an F-16A aircraft configuration at a freestream Mach number of 1.2, a Reynolds number of 12.75×10^6, and an angle of attack of 6 deg. The three-dimensional Navier-Stokes equations in mass-averaged variables were integrated numerically using the MacCormack explicit algorithm with an algebraic turbulence model to provide closure of the system of equations. The grid structure, boundary conditions, and solution procedure are discussed in detail for this complex aircraft geometry. The results are then compared to experimental data in terms of surface pressure coefficients, lift coefficient, and drag coefficient with reasonable agreement. Finally, details of the flow are discussed, such as the strake vortex and the wing vortex structures.

Nomenclature

CP = pressure coefficient, $[2(p - p_\infty)/\rho_\infty u_\infty^2]$
c = local speed of sound, $(\gamma RT)^{1/2}$
c_v = specific heat at constant volume
e = total specific energy, $c_v T + \frac{1}{2}(u^2 + v^2 + w^2)$
L = length of aircraft
p = pressure
Q = total velocity, $(u^2 + v^2 + w^2)^{1/2}$
S = arc length circumferentially around the body
T = temperature
t = time
U = vector of dependent variables
u,v,w = Cartesian velocity components in the x,y,z directions
x,y,z = Cartesian coordinates in streamwise, normal, and spanwise directions
y^+ = law of the wall coordinate
β = pressure damping coefficient
γ = specific heat ratio, 1.4 for air
μ = molecular viscosity coefficient
μ_t = turbulent viscosity coefficient
ξ,η,ζ = transformed spatial coordinates
ρ = density

Introduction

THE ultimate goal of computational aerodynamics is to develop a numerical methodology to predict accurately the flowfield about complex aerospace vehicles in a shortened design cycle. This goal is still unrealized at the present time. Computer hardware and algorithm development, however, have evolved enough that considerable progress is being made toward this goal. Viscous simulations have been performed for wing/body,[1] propulsion/afterbody,[2] and simplified aircraft configurations.[3-6] The next logical step would be the simulation of a complex aircraft geometry. The present analysis, then, describes the simulation of the flowfield about a F-16A fighter at a moderate angle of attack and supersonic Mach number.

Up to this time, researchers have used simplified geometries or simplified equations to model the flow about the F-16. Karman et al.[7] modeled the transonic flow about the F-16 using an Euler solver and a blocked grid. Reznick and Flores[4] presented an excellent analysis of the leading-edge vortices generated by a wing-strake-fuselage body derived from the F-16A using a combination Euler/thin-layer solver in the transonic flow regime. Flores et al.[5] also obtained a solution using the same solver for a simplified F-16A configuration at subsonic conditions. More recently, Flores et al.[6] included a flow-through inlet in the F-16A configuration and obtained good results for the flow in the inlet/diverter region.

The F-16A model used in this study was 1/9 scale of the full aircraft size, which corresponded to the wind-tunnel model size, and described the left-hand side of the aircraft. The configuration was "clean," that is no antennas, missile rails, missiles, or minor protuberances were modeled. The rest of the aircraft, with the exception of the ventral fin, the horizontal tail slot, the vertical tail slot, and the propulsion inlet lip, was modeled. Although recent investigators[4-6] have used zonal grid methods to discretize the physical space about the F-16, a global gird was used, thus avoiding the problems of zone interfacing but exacerbating the problem of grid resolution about complex shapes.

The F-16A flowfield was simulated for a freestream Mach number of 1.2 an angle of attack of 6 deg, and a Reynolds number based on aircraft body length of 12.75×10^6. A freestream temperature of 441.77°R (245.43 K) and a freestream pressure of 505.07 psf (24.18 kPa) was chosen to correspond to wind-tunnel conditions.

MacCormack's explicit predictor-corrector algorithm[8] was used to discretize the mass-averaged Navier-Stokes equations in general coordinates. This algorithm was implemented in a fully vectorized computer code called FDL3D, which has been successfully used to study a wide range of supersonic steady and unsteady problems.[9-11]

The goals of this study are threefold: 1) to show how the complex geometry of the F-16A was modeled in a global grid, 2) to verify the computation by comparison with experimental data, and 3) to further study the flowfield about the aircraft. To accomplish this, the governing equations and turbulence model are briefly covered and then the spatial discretization of the flowfield and the boundary conditions on the computational domain and on the aircraft surface are discussed. Next, the solution procedure is discussed with an emphasis on the methods used to obtain a solution with a minimum of computer time. The computational results are then verified by a comprehensive comparison to experimental pressure coefficients, lift coefficient, and drag coefficient. Finally, details of the flowfield, such as surface oil flow patterns, shock structures, and vortex formation, are qualitatively explored.

Received April 30, 1988; presented as Paper 88-2507 at the AIAA 6th Applied Aerodynamics Conference, Williamsberg, VA, June 6-8, 1988; revision received Jan. 6, 1989.

*Aerospace Engineer. Member AIAA.
†Aerospace Engineer. Associate Fellow AIAA.
‡Technical Manager. Associate Fellow AIAA.

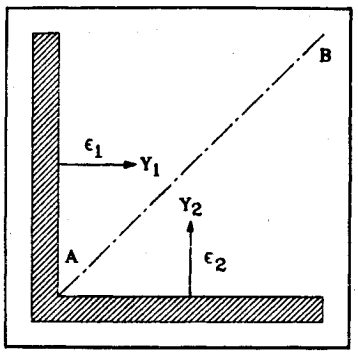

Fig. 1 Eddy viscosity representation for axial corner.

Governing Equations

The equations solved for this problem were the unsteady, compressible, three-dimensional Navier-Stokes equations written in mass-averaged variables, chain-rule conservative form, and general coordinates.

The effects of fine-scale turbulence were accounted for in the computation by specifying, as usual, a turbulent Prandtl number of 0.9[1,9-11] and using the two-layer, eddy viscosity formulation of Baldwin and Lomax[12] to close the system of equations. Because of the geometric complexity of the configuration, the Baldwin-Lomax model was modified in regions of the flowfield where multiple turbulent length scales were present. Typical of such regions are the streamwise axial corners formed by the intersection of the lower wing surface/fuselage and the vertical tail/fuselage. A schematic representation of these regions is shown in Fig. 1. Here, y_1 and y_2 are the normal distances, respectively, from the vertical and horizontal surfaces, and ϵ_1 and ϵ_2 are the corresponding eddy viscosity coefficients calculated for an isolated surface completely neglecting the presence of the other intersecting surface. The complete coefficient was then taken as the linear combination

$$\mu_t = \frac{y_2\epsilon_1 + y_1\epsilon_2}{y_1 + y_2}$$

Although this formulation has no physical basis, it does possess the following desirable properties:

1) The computation of more complex length scales is avoided.

2) As either surface is approached ($y_1 \to 0$ or $y_2 \to 0$), the model degenerates to the correct limiting form.

3) Along the bisector of the included angle between the surfaces (line A-B), $\mu_t = \frac{1}{2}(\epsilon_1 + \epsilon_2)$.

A major problem with computing the flow about complex geometries has been the generation of a grid system that accurately describes the geometry and provides the desired numerical resolution. As a base, the blocked grid generated by Kármán et al.[7] for an Euler solver was used. The grid blocks were first assembled into a global grid with an H-H type structure and then refined normal to the body surfaces in order to resolve the viscous regions. The refinement was done by using spline fits along constant coordinate lines and then distributing points along the arclength of the fitted line to provide the necessary point clustering. The original blocked grid was spatially continuous at block boundaries, but the slope of the coordinate lines were not necessarily continuous. In a global grid, this will lead to discontinuities in the grid metrics of the flowfield and may cause the solution to diverge. To avoid this problem, curve fitting was used to smooth the grid providing continuous metric values throughout the flowfield away from body surfaces.

The resulting grid has a global structure of 81 points by 97 points by 158 points (81 × 97 × 158) for a total of 1,241,406 points. The computational domain is shown in Fig. 2 and the surface grid is shown in Fig. 3. There were 135 points along the body in the streamwise direction, 37 points along the wing

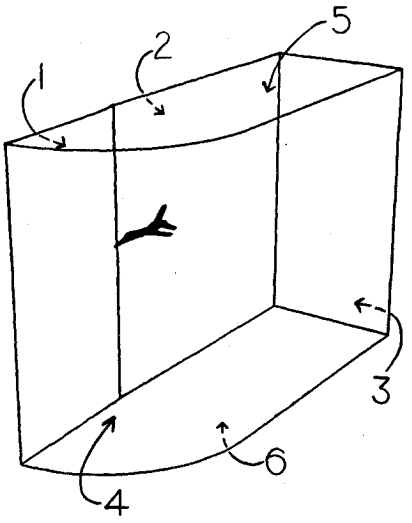

Fig. 2 Computational domain and boundary conditions.

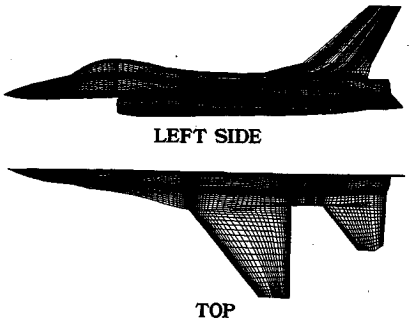

Fig. 3 Body surface grid.

in the streamwise direction, and 61 points from the symmetry plane to the wing tip. A total of 17,600 points were used to describe the surface of the aircraft. For the grid resolution normal to the body, a typical boundary-layer profile at the wing trailing edge had a thickness defined by approximately 15 points and a value of $y^+ = 7.78$ at the first grid point above the wing.

The use of a single global grid, as opposed to a multiblock zonal grid structure, was made possible by the availability of a computer with a large internal dynamic memory. This capacity allowed processing of all grid points within the flowfield at each time step, and eliminated the need for matching zonal solutions at interface boundaries. In addition, the true physical boundary conditions could rapidly influence the solution domain without being delayed by zonal boundaries.

Referring to Fig. 2, the boundary conditions on the domain were freestream along faces 4, 5, and 6, and on face 3 the following outflow conditions were used:

$$\frac{\partial(\rho)}{\partial\xi} = \frac{\partial(\rho u)}{\partial\xi} = \frac{\partial(\rho v)}{\partial\xi} = \frac{\partial(\rho w)}{\partial\xi} = \frac{\partial(\rho e)}{\partial\xi} = 0 \tag{1}$$

On the symmetry plane, faces 1 and 2, the following conditions were used:

$$\frac{\partial(\rho)}{\partial\zeta} = \frac{\partial(\rho u)}{\partial\zeta} = \frac{\partial(\rho v)}{\partial\zeta} = \frac{\partial(\rho e)}{\partial\zeta} = \rho w = 0 \tag{2}$$

On the body $u = v = w = 0$, with a constant wall temperature of 543.15°R (301.75 K), the wall pressure was calculated from

$$\frac{\partial(p)}{\partial\eta} = 0 \tag{3}$$

using a zeroth-order extrapolation. For the propulsion inlet, flow-through conditions [Eq. (1)] were used to approximate

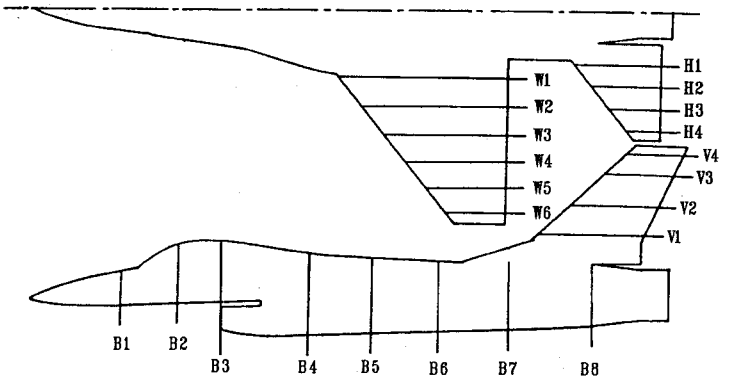

Fig. 4 Pressure comparison locations.

the wind-tunnel conditions. The environmental control inlet was also modeled on the F-16A and the boundary conditions used for this inlet were also flow-through.

Numerical Procedure

The steady-state solutions were obtained using the time-dependent, explicit, predictor-corrector finite-difference algorithm of MacCormack.[8] In order to suppress numerical oscillations caused by large gradients in the dependent variables, some numerical damping was added to the algorithm. The damping has the form as given by MacCormack and Baldwin[13]

$$\beta\Delta t\sum_{i=1}^{3}\Delta\nu_i^3\frac{\partial}{\partial\nu_i}\left[\frac{\partial U}{\partial\nu_i}\left|\frac{\partial^2 p}{\partial\nu_i^2}\right|\frac{|u_i+c|}{p}\right] \tag{4}$$

where $\nu_{1,2,3}=\xi,\eta,\zeta$ and $u_{1,2,3}=u,v,w$. This term is added to the conserved variable vector at the end of the predictor step and at the end of the corrector step. For the solutions presented here, a damping coefficient of $\beta=2.0$ was used.

The time step to maintain stability of the algorithm was calculated using the inviscid CFL condition with a viscous correction

$$\Delta t=\sigma\min(\Delta t_1,\Delta t_2,\Delta t_3) \tag{5}$$

The safety factor σ was usually chosen to be 0.3. In Eq. (5), Δt_1 is the inviscid time step, and Δt_2 and Δt_3 account for the viscous regions normal to the body in the η and ζ directions.[13]

Both time-accurate and local time steps were used to advance the solutions. In the time-accurate mode, the minimum time step in the flowfield was used for all points, whereas, in the local mode, the time step calculated at the point was used to advance the solution at that point. The usual procedure was to begin the calculation using the time-accurate mode, and after a few thousand iterations switch to the local mode to hasten convergence.

Because of the complexity of the software, we performed the calculations in two stages. The first stage involved calculating the flow using a "coarse" grid of $61\times60\times138$ points. This grid was used to debug the very complex boundary conditions and to provide a first solution. This coarse-grid solution was then interpolated to the "fine" grid of $81\times97\times158$ points, giving a better initial guess at the flowfield for the second-stage calculation.

Since the coarse-grid solution was used to start the fine-grid solution and local time steps were used to hasten the solution convergence, it was very difficult to monitor the convergence rate. To insure that the final solution converged, we monitored the boundary-layer velocity profile at the trailing edge of the wing for two spanwise stations and we also monitored the wing pressure coefficients for two spanwise stations. When the boundary-layer profiles and wing pressure coefficients varied by less than 1% over 1000 iterations, then the solution was considered converged. After 7000 iterations, the coarse-grid solution converged, and after 5000 iterations, the fine-grid solution converged.

Because of the large grid size and number of iterations required for convergence of the solution, a Cray 2 supercomputer was used to perform the calculations. For the coarse-grid solution, approximately 20 megawords of internal memory and 33 CPU h of time were necessary to obtain a converged solution. For the fine-grid solution, 59 megawords and 40 CPU h of Cray 2 time yielded a solution.

Results

First, the numerical results are compared to wind-tunnel data.[14] The wind-tunnel model contained the features that were neglected in the numerical model, i.e., the propulsion inlet lip, the ventral fins, the horizontal tail slot, and the vertical tail slot. Also, the wind-tunnel model included wing-tip missiles and missile launch rails. Wind-tunnel data, however, indicate that these features contribute only a small percentage to the lift and drag coefficients.[14] Since the pressure tap and grid-point locations did not coincide, the numerical data were linearly interpolated to the experimental data stations. Figure 4 shows the locations of the stations where data are available for comparison. The spanwise wing station is indicated by W, spanwise horizontal tail section by H, vertical tail station by V, and streamwise body station by B.

In Fig. 5, the experimental wing pressure coefficients are compared to the numerical wing pressure coefficients. In each plot, the upper curve corresponds to the wing upper surface and the lower curve corresponds to the wing lower surface. The solid line depicts the numerical data, and the solid circles depict the experimental data. In general, the numerical data agree favorably with the experimental data, especially on the lower surface of the wing. On the upper surface, however, the suction peak at the leading edge is not correctly predicted at any of the stations. This is caused by the lack of numerical resolution at the leading edge and the H-grid topology. Starting at station W2, there is an increasing difference in the data at the trailing edge of the upper surface. The difference seen near the upper surface trailing edge of the pressure coefficient plots is probably caused by the incorrect prediction of the trailing-edge compression, leading to a pressure rise sooner than indicated by the experimental results. Another disparity between the experimental and numerical data occurs at stations W5 and W6 near the wing tip. As mentioned earlier, the wind-tunnel model contained missiles and missile launch rails on the wing tip, which will inhibit the formation of the wing tip vortex and lead to the observed differences.

Figure 6 shows the pressure-coefficient plots for the upper and lower surfaces of the horizontal tail. At station H1, the numerical data compare poorly with the experimental data, presumably because the horizontal tail slot is not numerically modeled. Pressure comparisons at stations H2 and H3 are similar to the wing pressure comparisons—the lower surface compares very well and the leading and trailing edges of the upper surfaces show definite differences between experimental

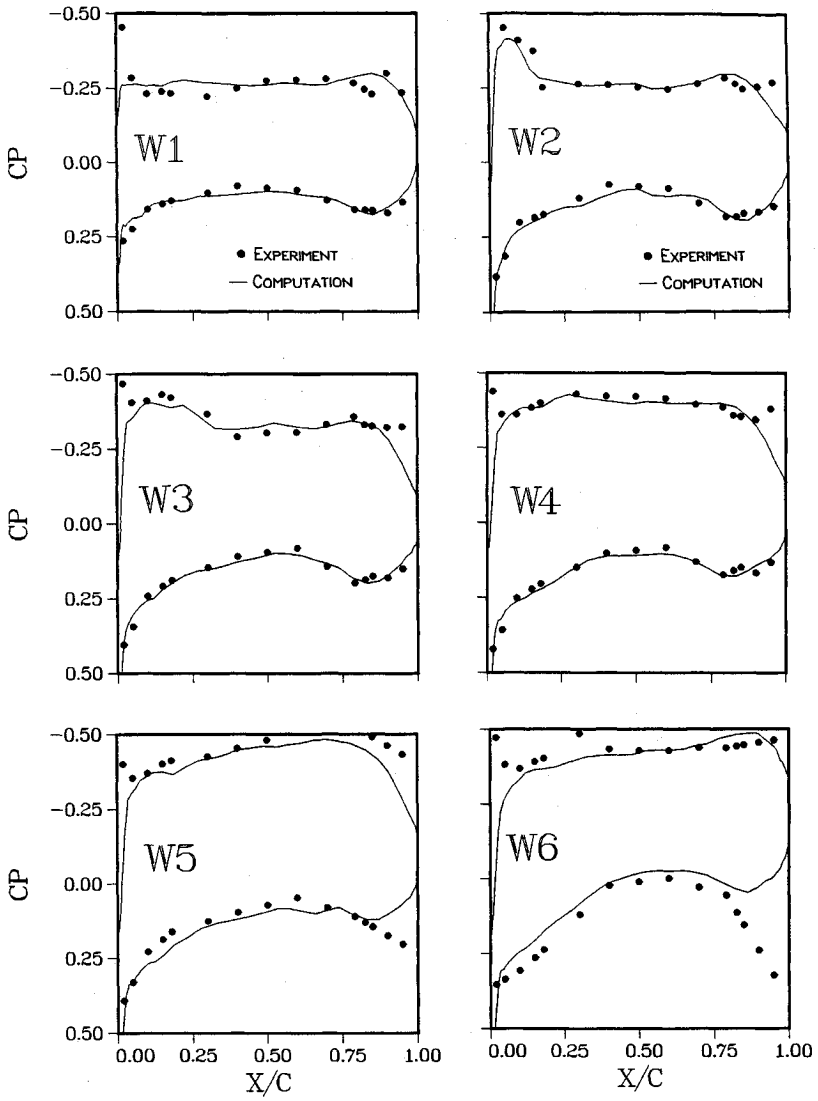

Fig. 5 Wing pressure comparison.

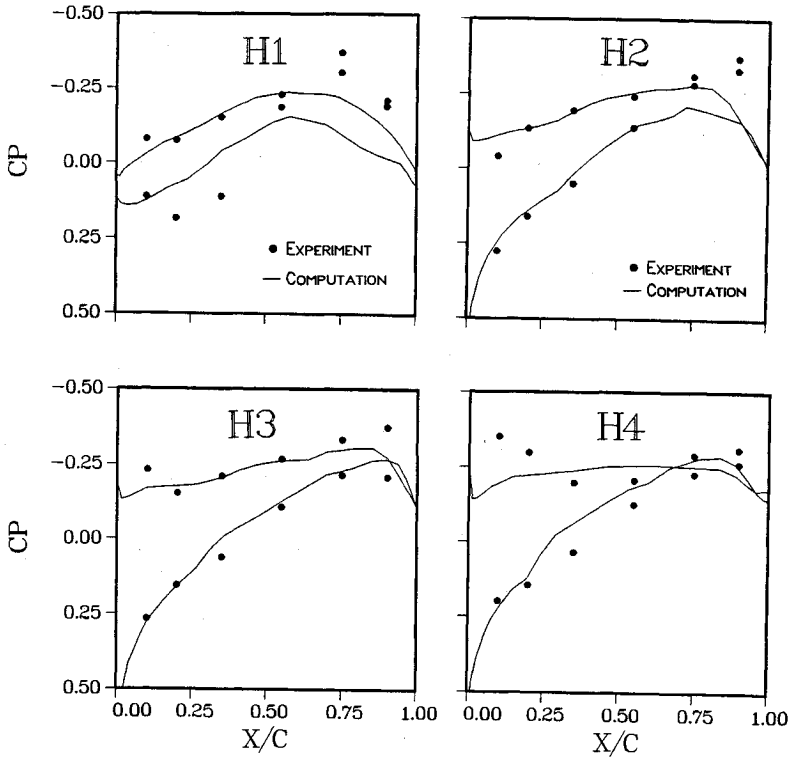

Fig. 6 Horizontal tail pressure comparison.

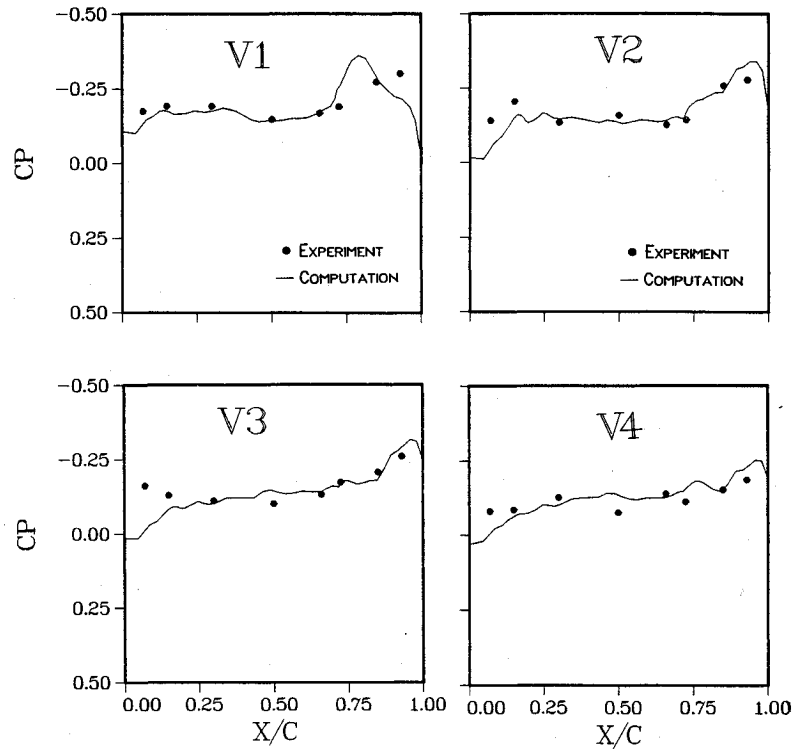

Fig. 7 Vertical tail pressure comparison.

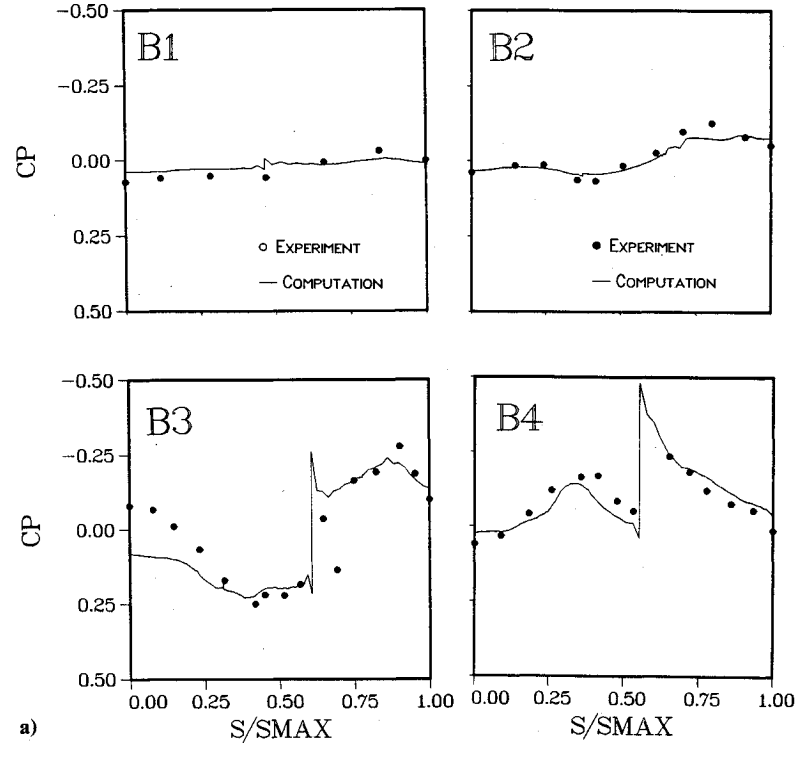

Fig. 8 Body pressure comparison.

a)

and numerical data. These differences are caused by the incorrect prediction of the trailing-edge compression, just as happened on the wing upper surface. At station H4, the comparison is worse and may be because of geometry differences between the numerical and wind-tunnel model.

The next plots (Fig. 7) compare the pressure coefficients at four stations on the vertical tail. Again, the comparison is reasonable except near the leading edge of the vertical tail. At station V1 near $X/C = 0.75$, there is an expansion and compression in the numerical data, but not in the experimental data. This inaccuracy was caused by an improper modeling of the vertical tail surface in the region of the slot.

Comparison of surface pressure distributions along body stations are presented as a function of arc length S in Figs. 8a and 8b. Here, the origin of the S coordinate is at the plane of symmetry on the underside of the body; S increases circumferentially around the body surface such that $SMAX$ occurs at the plane of symmetry on the top of the body. The sudden decrease in CP observed at stations B3 and B4 near $S/SMAX = 0.6$ are caused by the strake (see Fig. 3). It should be noted that a shock wave is present in the flowfield ahead of the propulsion inlet. The strength and location of this shock will be determined by the inlet lip and the inlet flow conditions. Because the inlet lip was not modeled numerically and

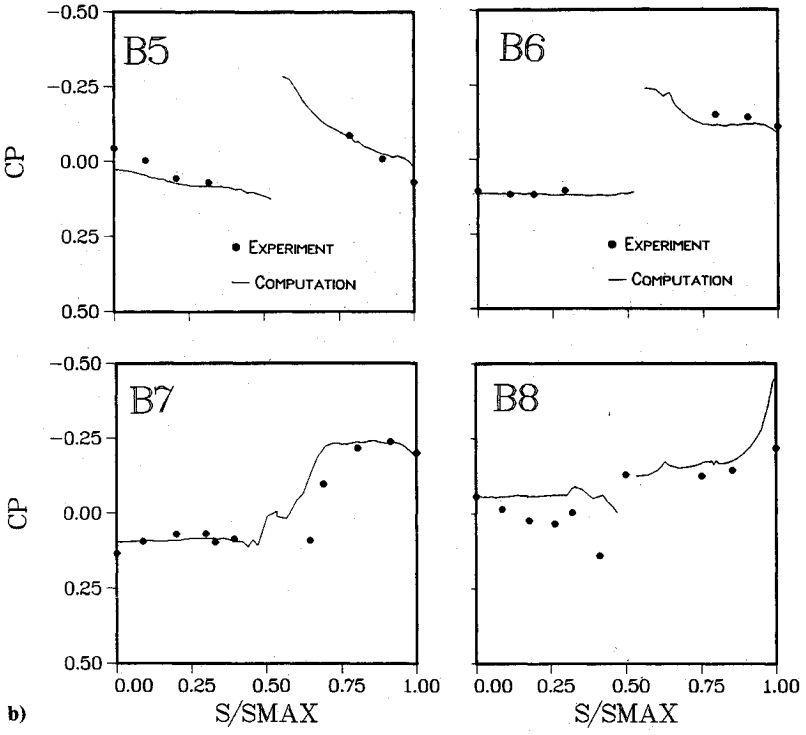

Fig. 8 (con't) Body pressure comparison.

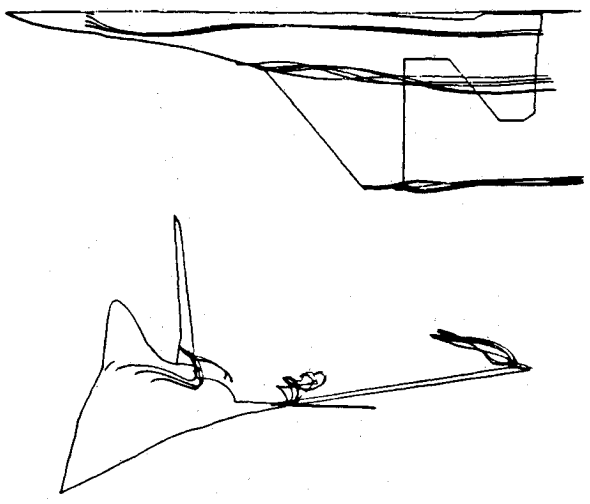

Fig. 9 Particle paths.

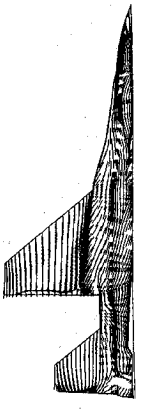

Fig. 10 Upper-surface simulated oil-flow patterns.

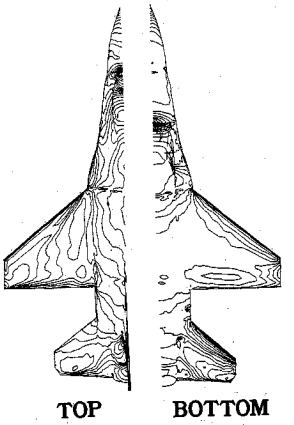

Fig. 11 Surface pressure contours.

because it was not possible to duplicate the inlet test conditions numerically, some disparity of results close to the inlet are expected. These effects can be noted near the plane of symmetry ($S/SMAX = 0$) in the result at station B3. Stations B5 and B6 represent body locations where the wing emerges from the body. The break in the curves at these stations indicates points at the lower and upper surfaces, respectively. A similar situation exists with regard to the horizontal tail at station B8. The aforementioned abrupt change in geometry near the base of the vertical tail results in the disparity observed near $S/SMAX = 1.0$ at station B8.

Figure 9 indicates the paths of fluid particles that originate immediately upstream of the canopy, the strake/wing intersection, and the wing tip. The flow along these pathlines is seen to produce a vortical structure as the particles move downstream. Particles passing over the strake and wing tip are forced up and away from the surface. Because of supersonic flow conditions, the helical motion of these pathlines terminates rapidly as the particles attain freestream conditions. No vortical structures were observed leaving the vertical and horizontal tails.

Upper-surface simulated oil flow patterns are presented in Fig. 10. The lines of the vortices leaving the surface at the canopy and at the wing/strake intersection, which were displayed in Fig. 9, are visible. Also apparent are separation lines near the trailing edges of the wing and the horizontal tail, which were not observed in experimental oil flow diagrams of

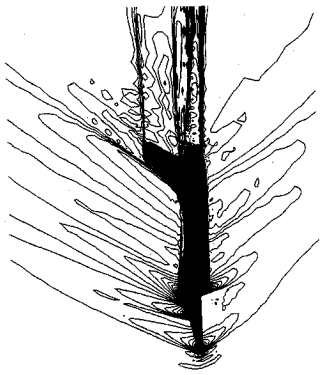

Fig. 12 Density contours on symmetry plane.

Table 1 Lift and drag coefficients

	Computation	Experiment	Difference,%
C_L	0.504	0.480	5.0
C_D	0.0783	0.0830	5.6

a similar configuration at the same flow conditions. The separation may be caused by insufficient grid resolution normal to the body or improper grid topology, which causes the eddy viscosity to be underpredicted.

Pressure contours on the upper and lower surfaces and density contours on the plane of symmetry are displayed in Figs. 11 and 12, respectively. Shock waves at the body nose, ahead of the canopy and propulsion inlet, are evident. Shock waves are also apparent along the leading edges of the wing and vertical tail. Low-pressure regions can be observed behind the canopy and at the wing trailing edge.

As another measure of the overall accuracy of the present results, the lift and drag coefficients were calculated for comparison with the wind-tunnel measurements. The lift and drag coefficients, given in Table 1, were calculated from the computed surface stress tensor integrated over the body using Simpson's rule. The 5.0% difference between the lift coefficients and 5.6% difference between the drag coefficients is well within the data scatter band of the wind-tunnel results.

Conclusions and Discussion

A numerical simulation has been presented for the steady flow over an F-16A aircraft configuration at a freestream Mach number of 1.2, a Reynolds number of 12.75×10^6, and an angle of attack of 6 deg. The numerically generated surface pressure distributions were found to compare well with measured data. Disparities between the computation and experiment were produced by differences in the respective geometric configurations and inadequate numerical resolution in some regions, most notably at the leading and trailing edges of the wing and horizontal tail. Despite these minor inaccuracies, the lift and drag coefficients were calculated within 5% of the wind-tunnel values.

Obviously, the dream of the "numerical wind tunnel" has not been realized yet. But, with improvements in algorithms and in computer speed, this day may not be too far in the future.

Acknowledgments

Computer resources for this work were provided by the National Aerodynamic Simulator facility, NASA Ames Research Center, Moffett Field, California. The authors are also grateful to Jeff Graham for his work on the grid, and to George Howell of General Dynamics, Fort Worth Division, for his help in obtaining the experimental data.

References

[1]Shang, J. S., "Numerical Simulation of Wing-Fuselage Aerodynamic Interaction," *AIAA Journal,* Vol. 22, Oct. 1984, pp. 1345-1353.

[2]Deiwert, G. S., Andrews, A. E., and Nakahashi, K., "Theoretical Analysis of Aircraft Afterbody Flow," AIAA Paper 84-1524, June 1984.

[3]Obayashi, S., Fujee, K., and Takanashi, S., "Toward the Navier-Stokes Analysis of Transport Aircraft Configurations," AIAA Paper 87-0428, Jan. 1987.

[4]Reznick, S. G. and Flores, J., "Strake-Generated Vortex Interactions for a Fighter-Like Configuration," AIAA Paper 87-0589, Jan. 1987; also, *Journal of Aircraft,* Vol. 26, April 1989, pp. 289-294.

[5]Flores, J., Reznick, S. G., Holst, T. L., and Gundy, K., "Transonic Navier-Stokes Solutions for a Fighter-Like Configuration," AIAA Paper 87-0032, Jan. 1987; also, *Journal of Aircraft,* Vol. 25, Oct. 1988, pp. 875-881.

[6]Flores, J., Chaderjian, N. M., and Sorenson, R. L., "Simulation of Transonic Viscous Flow Over a Fighter-Like Configuration Including Inlet," AIAA Paper 87-1199, June 1987; also, *Journal of Aircraft,* Vol. 26, April 1989, pp. 295-301.

[7]Karman, S. L., Steinbrenner, J. P., and Kisielewski, K. M., "Analysis of the F-16 Flowfield by a Block Grid Euler Approach," AGARD Paper No. 18, 58th Meeting of the Fluid Dynamics Panel Symposium on Applications of Computational Fluid Dynamics in Aeronautics, 1986.

[8]MacCormack, R. W., "The Effect of Viscosity in Hypervelocity Impact Cratering," AIAA Paper 69-354, April 1969.

[9]Shang, J. S. and Scherr, S. J., "Navier-Stokes Solution for a Complete Re-Entry Configuration," *Journal of Aircraft,* Vol. 23, Dec. 1986, pp. 881-888.

[10]Shang, J. S., McMaster, D. L., Scaggs, N., and Buck, M., "Interaction of Jet in Hypersonic Cross Stream," AIAA Paper 87-0055, Jan. 1987.

[11]Rizzetta, D. P., "Numerical Simulation of Supersonic Flow Over a Three-Dimensional Cavity," AIAA Paper 87-1288, June 1987.

[12]Baldwin, B. S. and Lomax, H., "Thin-Layer Approximation and Algebraic Model for Separated Turbulent Flows," AIAA Paper 78-257, Jan. 1978.

[13]MacCormack, R. W. and Baldwin, B. S., "A Numerical Method for Solving the Navier-Stokes Equations with Application to Shock-Boundary Layer Interactions," AIAA Paper 75-1, Jan. 1975.

[14]Reue, G. L., Doverenz, M. E., and Wilkins, D. D., "Component Aerodynamic Load from 1/9-Scale F-16A Loads Model," General Dynamics, Fort Worth, TX, Rept. 16PR316, May 1976.